

Simple Performance Modeling of a Radio-Frequency Ion Thruster

IEPC-2007-072

Presented at the 30th International Electric Propulsion Conference, Florence, Italy
September 17-20, 2007

Michael M. Tsay* and Manuel Martinez-Sanchez.†
Massachusetts Institute of Technology, Cambridge, MA, 02139, U.S.A.

Abstract: A simple performance model is developed for an inductively-coupled plasma (ICP) discharge, radio-frequency (RF) ion thruster. Methods of particle and energy balance are utilized for modeling the ICP discharge. A lumped-element circuit analysis, a transformer model, and a transmission line model are incorporated in the equations of energy balance for estimating the absorbed power by the plasma. In the transformer model, the short solenoid is treated as a two-turn primary coil and the plasma as a one-turn secondary air coil. The primary and mutual inductance are approximated by theories of single-layer coils. The ICP discharge model is successful in predicting the resonant frequency of the system with accuracy within 0.01 MHz. The reflected power of the system is predicted with accuracy within 30% and its trend is also validated. The anode current of the thruster is estimated by a simple one-dimensional ion extraction model, which yields accuracy within 10% of the measured values.

Nomenclature

k	= Boltzmann's constant
R	= Chamber radius
L	= Chamber length
σ	= Plasma conductivity
δ	= Skin depth
ω	= Driving frequency
ρ	= Reflection coefficient
m_i	= Ion mass
n_e	= Electron density
n_n	= Neutral density
T_e	= Electron temperature
ν_{eff}	= Effective elastic collision frequency for electrons
ν_{ion}	= Ionization frequency
σ_{en}	= Electron-neutral total scattering cross section
u_B	= Bohm velocity
V_{total}	= Applied inter-grid potential
ϕ_i	= Ion transparency of the grid
ϕ_w	= Potential drop across the sheath at the wall

* Doctoral student, Department of Aeronautics and Astronautics, mmsay@mit.edu.

† Professor, Department of Aeronautics and Astronautics, mmart@mit.edu.

I. Introduction

A. Project background

ICP RF ion thrusters were first invented at the Giessen University of Germany in the 1960s. Since then, the European Aeronautic Defense and Space Company (EADS) Space Transportation GmbH and its industrial support, the German Astrium GmbH group, have adapted this concept and successfully developed a family of space-qualified RF thrusters known as the Radio-frequency Ion Thruster (RIT) series.¹ This type of ion thrusters have since shared a history of successful flight operations.

ICP RF ion thrusters are very similar to the traditional direct-current (DC) bombardment-type ion thrusters in terms of their electrostatic ion acceleration mechanism. The major difference between them is, unlike their DC counterparts, the ICP RF ion thrusters utilize electromagnetic fields induced by high-frequency coil currents to achieve and sustain ionization. During such process, the magnetic fields induced by the RF coil and the azimuthal plasma current are coupled, thus receiving its name of inductively-coupled ion thruster. Due to the absence of the life-limiting internal hot cathode, the ICP RF ion thrusters have the potential to achieve long operational life while preserving other favorable characteristics of a typical DC ion thruster such as high specific impulse (>3000 seconds), high propellant utilization ($>85\%$), and high electric efficiency ($>80\%$).²

B. Project motivation and objectives

This project is motivated by the simple performance model developed for DC ion thrusters by Brophy and Wilbur in 1980s. This model, well known as the Brophy's model, consists of a particle and energy balance calculation that relates thruster performance to adjustable operational parameters such as mass flow rate and discharge potential.³ Inspired by Brophy's approach, we decided to use similar method to model the ICP RF ion thruster. Our objective is to develop a simple one-dimensional zero-th order mathematical model that can capture the physics of an ICP discharge, analyze and optimize the matching network, and ultimately predict the thruster performance.

The results of our model are validated with the experimental data provided by Busek Co., Inc. The experimental subject, shown in Fig. 1, is a proof-of-concept version of the RF ion thruster developed by Busek. This prototype design resembles the configuration of a German RIT series thruster with the screen grid serving as anode and xenon as propellant. A capacitive matching network was placed in parallel with the coil circuit. In the experiments, source frequency was adjusted to seek resonance at each operating condition.

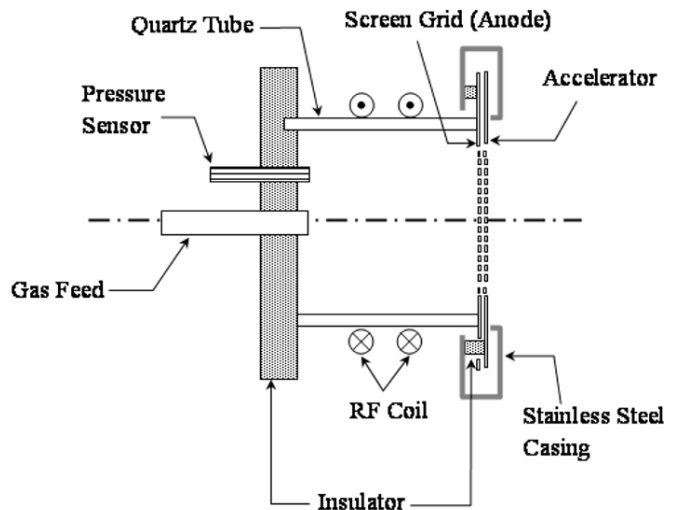


Figure 1. Conceptual arrangement of the ICP RF ion thruster. Figure does not bear dimensional accuracy.

II. Theory

The theory section contains three major parts: the ICP discharge model, a matching circuit analysis, and a discussion on the ion extraction model. In the ICP discharge model, bulk plasma properties are calculated by means of a particle balance and an energy balance. The matching circuit analysis is used for calculating the RF power absorbed by the plasma, as well as for predicting the resonant frequency and the reflected power. We include a simple one-dimensional ion extraction model for comparison with the anode current data taken from experiments.

A. Inductively-coupled plasma discharge model

The ICP discharge model is developed based on a similar model published in 1994 by Lieberman and Gottscho. In our model, electron density is considered to be volume-averaged and electron temperature is assumed to be

uniform. In addition, we assume that electrons are Maxwellian distributed and heavy particles are thermalized with the wall.

1. Particle balance and solution for electron temperature

The electron temperature in an ICP RF ion thruster is usually kept low (less than 5eV). This feature is very similar to the one in a DC ion thruster and is very attractive because the electrons are energetic enough to initiate ionization but do not possess much excess energy to cause significant power loss to the anode or a large beam divergence. The solution for electron temperature can be found by means of a particle balance when the chamber geometry, wall temperature, and background neutral density are specified. Because we usually do not have direct knowledge of the neutral density, we have to use iterative methods for carrying out this ICP discharge model. In the model described by Lieberman and Gottscho, the governing equation for calculating the electron temperature is derived by assuming that ions and electrons only recombine at the wall. Particle balance is then achieved by equating the ionization rate to the diffusion loss rate to the walls,⁴

$$\nu_{ion} = u_B / d_{eff} = \sqrt{kT_e / m_i} / d_{eff} \quad (1)$$

where ν_{ion} is the ionization frequency and the right-hand side of Eq. 1 describes the rate of particle loss due to Bohm diffusion. It is a little counter-intuitive to use a particle balance equation to solve for electron temperature instead of density. However, it can easily be observed that the electron density term does not even appear in our particle balance equation. The effective plasma size for diffusion, shown in Eq. 1, is written as⁴

$$d_{eff} = RL / [2(Rh_L + Lh_R)] \quad (2)$$

where R is the inner radius, L is the chamber length, h_L and h_R are the normalized axial and radial sheath edge densities presented as⁴

$$h_L = n_{sheath,L} / n_0 = 0.86 / [3 + (L / 2\lambda_i) + (0.86Lu_B / \pi\gamma D_i)^2]^{1/2} \quad (3)$$

$$h_R = n_{sheath,R} / n_0 = 0.8 / [4 + (R / \lambda_i) + (0.8Ru_B / 2.405J_1(2.405)\gamma D_i)^2]^{1/2} \quad (4)$$

with J_1 being the Bessel function of the first kind and the parameters $\lambda_i = 1 / (n_n \sigma_{in})$, $\gamma = T_e / T_i$, and $D_i = kT_e / (m_i \nu_{in})$ representing respectively the mean-free-path for ions, the ratio between electron and ion temperature, and the ion diffusion coefficient. The ion-neutral scattering cross section required for computing the ion-neutral scattering frequency, ν_{in} , and the mean-free-path of ion is calculated from Banks' formula⁵

$$\sigma_{in} = 8.28072 \times 10^{-16} / c_r, \quad [\text{m}^2] \quad (5)$$

where c_r is the relative velocity between singly-charged ions and background neutrals upon elastic collision derived from the reduced mass. Returning to Eq. 1, now we derive the ionization frequency, ν_{ion} , from the definition of ionization rate,⁶

$$\dot{n}_e = \nu_{ion} n_e = n_n n_e \int_0^\infty f_e c \sigma_{ion}(c) 4\pi c^2 dc \quad (6)$$

where f_e is the Maxwellian distribution function and σ_{ion} is the ionization cross section. Inside our ICP discharge, the bulk electron temperature is less than the first ionization energy (12.1eV for Xenon) and only a small group of electrons possess energy exceeding the ionization threshold. Therefore, we can consider only the linear part of the ionization cross section curve near the threshold and then carry out the integration either algebraically or numerically.⁶

2. Plasma conductivity and skin depth

In ICP discharges, the coil-induced magnetic field does not penetrate fully into the plasma. The spatial decay constant of a normally incident electromagnetic wave within the plasma is often referred to as the "skin depth" and it is inversely related to the driving frequency.⁶ The term "skin depth" does not imply the absence of magnetic field beyond it; it merely characterizes the weakening of magnetic field. In the extreme cases of high frequency and high pressure, ionization only occurs within the very thin skin layer of plasma near the wall and the discharge is difficult to be sustained; this phenomenon is known as the "skin effect." On the other hand, large skin depth is also unfavorable because an increase in magnetic field penetration corresponds to insufficient ionization in the chamber. As the result, the skin depth of a sustainable ICP discharge is usually in the order of 1/4 to 1/3 of the inner radius.

Although the skin effect is not strong in our ICP RF ion thruster, it is an essential element in modeling the plasma resistance and ultimately can affect the energy balance equation.

In our model, we derive the expression for skin depth by first modeling the core plasma as a conductor with uniform conductivity

$$\sigma = e^2 n_e / (m_e v_{eff}) \quad (7)$$

The effective elastic collision frequency, v_{eff} , includes both electron-neutral scattering and Coulomb collisions

$$v_{eff} = v_{en} + v_{ei} = \bar{c}_e n_n \sigma_{en} + \bar{c}_e n_i \sigma_{ei} \quad (8)$$

where \bar{c}_e is the mean thermal velocity of electrons.

If assuming isotropic and Maxwellian-distributed electrons with uniform temperature, the electron-neutral scattering cross section can be found as a function of electron temperature by integrating the Maxwellian energy distribution function

$$\sigma_{en}(T_e) = \int f(E) Q_{en}(E) c dE / \bar{c}_e \quad (9)$$

where $Q_{en}(E)$ is the scattering cross section of atomic Xenon as a function of electron energy. In our model, Eq. 9 is numerically integrated with the data of atomic cross section obtained from Ref. 7; the result is shown in Fig. 2.

Now, assuming constant conductivity and no Hall effect, the penetration of magnetic field can be analyzed by solving its radial diffusion equation

$$\frac{\partial \bar{B}}{\partial t} = D_m \nabla^2 \bar{B} \quad (10)$$

where $D_m = 1/(\sigma \mu_0)$ is often referred to as the coefficient of magnetic field diffusion or magnetic diffusivity. Consider the complex notation for the axial magnetic field, $B(r,t) = \text{Re}[B(r) \exp(i\omega t)]$, Eq. 10 can be rewritten as

$$\eta^2 \frac{d^2 B}{d\eta^2} + \eta \frac{dB}{d\eta} - i\eta^2 B = 0, \text{ where } \eta = r / \sqrt{D_m / \omega} \quad (11)$$

Because we define the skin depth as the characteristic diffusion distance of the magnetic field, it makes sense to express the skin depth as

$$\delta = \sqrt{D_m / \omega} = \sqrt{1/(\omega \sigma \mu_0)} \quad (12)$$

and we can see that as either the plasma density (thus conductivity) or the frequency increases, the skin depth decreases.

3. Energy balance and solution for electron density

In addition to the particle balance, an energy balance is essential to characterize the ICP discharge. The electron density, which does not appear in the particle balance equation, can be computed from this energy balance. We balance the energy by assuming that all the absorbed power by the plasma is lost due to elastic collision, ionization and excitation in the discharge, and wall losses.⁸

$$P_{abs} = V_{chamber} \left[n_e v_{eff} (3m_e / m_n) k (T_e - T_n) + (n_e v_{ion}) eV_i' \right] + P_{wall} \quad (13)$$

where P_{abs} is the absorbed power, $V_{chamber}$ is the discharge volume, v_{eff} is the effective elastic collision frequency, $(n_e v_{ion})$ is the ionization rate discussed in Eq. 6, and eV_i' contains the energy expenditure due to ionization and excitation. The term eV_i' is approximately two to three times of the first ionization energy eV_i depending on the electron temperature. For better estimation, we can conduct Maxwellian-averaging on the ionization and excitation rate for a given electron temperature. By examination, the power loss due to elastic collisions (first term in the bracket) is relatively insignificant when compared to the eV_i' term; one can therefore choose to neglect it.

The wall loss term seen in Eq. 13 is the direct electron energy loss to the wall and is defined as

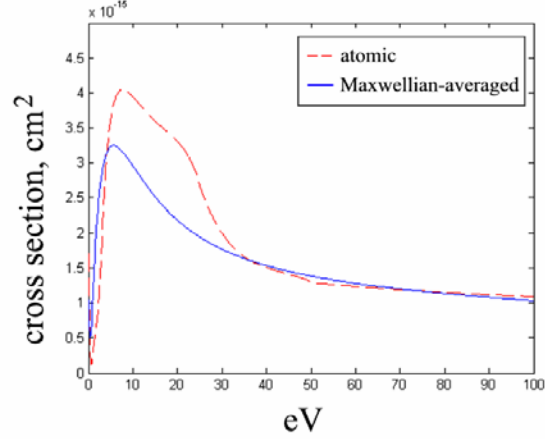


Figure 2. Electron-neutral total scattering cross section. Atomic cross sections are with respect to electron energy and averaged cross sections are with respect to electron temperature in units of eV.

$$P_{\text{wall}} = [A_{\text{wall}}(W_e + e\phi_w) + A_{\text{grid}}(W_e + e\phi_w(1 - \phi_i))] \cdot n_e u_B \exp(-1/2) \quad (14)$$

where A_{wall} is the surface area of the dielectric wall, A_{grid} is the area of the grid, and ϕ_i is the ion transparency of the grid. The average kinetic energy per electron lost to the wall is⁹

$$W_e = 2kT_e \quad (15)$$

Before the electrons surrender their energy of $2kT_e$ to the wall, some of their energy was exchanged with the ions when crossing the sheath potential. As the result, the electrons lose their kinetic energy at the sheath while the ions gain kinetic energy. This energy, carried by the ions, is considered lost when the ions impact the wall and recombine to form neutrals. The sheath potential across which the ions accelerate is found by equating the flux of ions to the one of electrons,

$$\phi_w = kT_e/e \ln \left[\sqrt{m_i/m_e} \sqrt{8/\pi} / (4 \exp(-0.5)) \right] \cong 5.77 kT_e/e \quad (\text{for Xenon}) \quad (16)$$

By examining Eq. 13 and 14, we found that the wall loss is actually a very important aspect in the design of ion thrusters because it can decrease the plasma density by taking away a significant portion of the absorbed power that could otherwise contribute to ionization.

With the use of Eq. 13, if the electron temperature and the absorbed power are prescribed, we can calculate the electron density. The underlying problem is that the absorbed power depends strongly on both electron temperature and density. In addition to an iterative method, a circuit analysis is needed in order to estimate the effect of chamber plasma on the primary circuit. By computing the plasma resistance and transforming such resistance into the primary circuit, its resistive power dissipation can be found. We can then assume this resistive power loss on the primary circuit to be the same as the absorbed power by the plasma. This technique is discussed in the next section.

B. Matching circuit analysis

The matching circuit analysis is based on lumped-element circuit theory and consists of a transformer model and a transmission line model. We first use the transformer model to represent the plasma loading on the primary circuit, and then use the transmission line model to calculate the power dissipation by this plasma element, thus completing the energy balance equation shown in the previous section. The transmission line model is important to our IPC discharge model because it can also be used to compare with the data on reflected power and resonant frequency obtained in experiments.

1. Transformer model of an ICP discharge

The idea of modeling an ICP discharge as a transformer with the plasma being a one-turn secondary coil is not new. A modified version of the model previously developed by Lieberman and Gottscho⁴ is presented here. Figure 3a shows the circuit diagram of our model where a parallel LC network is used in the primary circuit for impedance matching. The capacitor is also modeled with an equivalent series resistance (ESR), but it does not appear in Fig. 3. The main objective of this transformer model is to calculate the resistive power dissipation due to plasma loading, which is shown in Fig. 3b as element R_2 in the equivalent circuit.

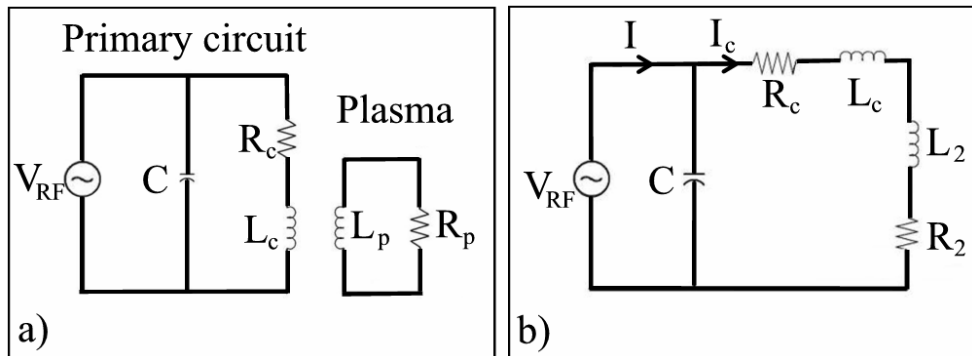


Figure 3. Circuit diagram of the transformer model. a) Primary circuit has capacitance C , coil resistance R_c and coil inductance L_c . Plasma has inductance L_p and resistance R_p . b) Equivalent circuit. The change of inductance in the primary circuit due to plasma loading is L_2 and the change of resistance is R_2 .

A major part of any transformer calculation is to figure out the correct representation for geometrical inductance and mutual inductance because they have profound influence on the coupling between the primary and the secondary circuits. We model the self-inductance of a short N -turn coil with the expression for single-layer coils in cylindrical winding form,¹⁰

$$L_c = 0.002\pi(D_w \cdot 100)(N^2) \left[\ln(4OD/l_c) - 1/2 \right] (10^{-6}), \quad [H] \quad (17)$$

where D_w is the winding diameter and l_c is the length of the coil, both in units of m^2 . The mutual inductance is then approximated with the expression for a solenoid with a coaxial circular filament,¹⁰

$$L_m = 0.0095N_1N_2 \left[(D_{w,2} \cdot 100)^2 / \sqrt{(D_{w,1} \cdot 100)^2 + (l_c \cdot 100)^2} \right] (10^{-6}), \quad [H] \quad (18)$$

where the subscript 1 and 2 represent the primary and the secondary coil.

In our transformer model, the plasma resistance is related to the plasma conductivity and skin depth,⁴

$$R_p = l_{path} / (\sigma A_{path}) = 2\pi R / (\sigma L \delta) \quad (19)$$

where σ is the conductivity, δ is the skin depth, R and L are the chamber inner radius and length. The self-inductance of the plasma consists of geometrical inductance and inductance arising from the electron inertia. Since we model the plasma as a one-turn air coil, its geometrical inductance can be expressed in a similar fashion as Eq. 17. The “winding radius” of our plasma coil is taken as 2/3 of the inner chamber radius since the skin depth of the plasma is observed to be within 1/3 of the inner radius. The inertia inductance of the plasma is estimated as⁴

$$L_{p,inertia} \cong R_p / \nu_{eff} \quad (20)$$

where ν_{eff} is the effective elastic collision frequency of the electrons. Once all these quantities are calculated, we can refer to Fig. 3 and proceed to evaluate the changes of resistance and inductance on the primary circuit due to plasma loading,

$$R_2 = \omega^2 L_m^2 R_p / [R_p^2 + (\omega L_p)^2] \quad (21)$$

$$L_2 = -\omega^2 L_m^2 L_p / [R_p^2 + (\omega L_p)^2] \quad (22)$$

With the use of complex impedance representations for circuit elements shown in Fig. 3b and a transmission line model, we can compute the coil current I_c and figure out the RMS power dissipation due to circuit element R_2 . This power dissipation is then considered to be the absorbed power of the plasma and can be used to complete Eq. 13.

2. Transmission line model

In high-frequency AC circuits, voltage and current often travel at different phase due to wave reflections. Impedance matching among the source, the transmission line, and the load is therefore an important design aspect for delivering maximum power to the load and minimizing the reflected power. Figure 4 illustrates such impedance matching.

In practice, RF power supplies usually come with an internal impedance of 50Ω and coaxial cables usually have a matching impedance of 50Ω as well. With the use of a directional coupler at the coaxial cable near the source, we can measure the reflected power due to unmatched load. Notice here that the “load” refers to all the circuit elements shown in Fig. 3b instead of the plasma load alone. Since the load impedance Z_{load} , shown in Fig. 4, is a function of driving frequency, we can find the frequency at which the reflected power is at its minimum. For our RF circuit, this condition is known as “resonance” and the corresponding frequency is referred to as the “resonant frequency.” The goals of our circuit model are to predict such resonant frequency, the reflected power at the resonant condition, and the power dissipation by

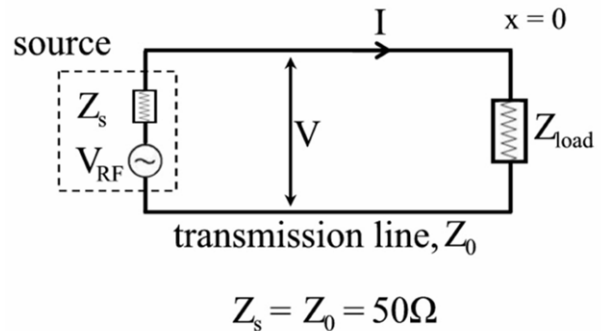


Figure 4. Circuit diagram of impedance matching. The load impedance Z_{load} represents the impedance of the entire circuit elements show in Fig. 3b.

the R_2 element shown in Fig. 3b.

Referring to Fig. 4, we can write the voltage and the current on the transmission line in terms of their forward and backward components and the line's characteristic impedance Z_0 ,¹¹

$$V(x) = V_+ \exp[i(\omega t - kx)] + V_- \exp[i(\omega t + kx)] \quad (23)$$

$$I(x) = (V_+/Z_0) \exp[i(\omega t - kx)] - (V_-/Z_0) \exp[i(\omega t + kx)] \quad (24)$$

with k here being the wave number. Combining these two equations, we can find the relationship between the forward and backward voltages by applying Ohm's law at the load,

$$Z_{load} = V_{x=0} / I_{x=0} = (V_+ + V_-) / (I_+ - I_-) = Z_0 (V_+ + V_-) / (V_+ - V_-) \quad (25)$$

$$\Downarrow$$

$$V_- = V_+ [(Z_{load} - Z_0) / (Z_{load} + Z_0)]$$

Because the reflected wave is measurable with a directional coupler, we can define a reflection coefficient ρ such that

$$\rho = V_- / V_+ = \sqrt{P_- / P_+} = (Z_{load} - Z_0) / (Z_{load} + Z_0) \quad (26)$$

where P_+ and P_- are the forward and backward power. By combining Eq. 24 and 25, we can find the current reaching the load as

$$I = I_+ - I_- = (V_+ - V_-) / Z_0 = V_+ / Z_0 \cdot [1 - (Z_{load} - Z_0) / (Z_{load} + Z_0)] \quad (27)$$

Referring to Fig. 3b, we can then use the current divider law to find the coil current I_c and calculate the RMS power dissipation by element R_2 , thus completing the energy balance equation in our ICP discharge model. The forward voltage seen in Eq. 27 is related to the observable forward power and the source impedance,

$$\langle P_+ \rangle = 1/2 \cdot (V_{+,peak}^2 / Z_s) \quad (28)$$

where $\langle P_+ \rangle$ describes the time-averaged forward power and is usually observable in the power supply's output screen. With Eq. 27 and 28, we can simply use the forward power as the adjustable input parameter and carry out our ICP discharge calculations.

C. Ion extraction

Since an ICP RF ion thruster relies on an electrostatic field for accelerating ions and generating thrust, it is essential to investigate the relationship between the applied inter-grid potential and the extractable ion current. The ion beam current also plays a major role in our ICP discharge model for establishing the steady-state chamber pressure, since we choose the operable flow rate, rather than pressure, as one of our input parameters. In classical theory, the absolute maximum of extractable ion current density is described by the Child-Langmuir space-charge limited current,¹²

$$j_{beam} = 4\sqrt{2}/9 [\epsilon_0 (e/m_i)]^{1/2} (V_{total}^{3/2} / l_g^2) \quad (29)$$

where ϵ_0 is the permittivity of free space, V_{total} is the applied inter-grid potential, and l_g is the grid spacing. The Child-Langmuir current assumes sufficient plasma production in the chamber for facilitating ion current saturation. This condition, however, is rarely reached in an ion thruster operation. In practice, the maximum extractable ion current is dominated by the impingement-limited perveance, which is a modified version of the Child-Langmuir current.¹³⁻¹⁵ This perveance term is not limited by the space-charge effect, but by the condition when the accelerator current starts to rise above 5% of the anode current due to direct ion impingement on the accelerator grid. Although useful for determining the boundaries of operation, the impingement-limited perveance is still an upper

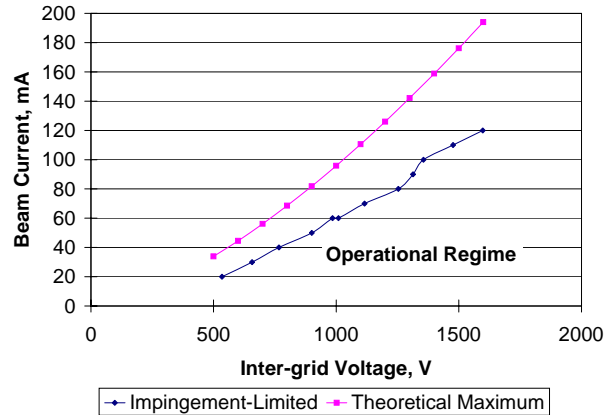


Figure 5. Operational limits of ion extraction.

bound of extractable current and does not give predictions on the beam current when the plasma production is below the nominal point. Figure 5 illustrates the limits of operation of a typical ion thruster that includes both the theoretical maximum (Child-Langmuir current) and the impingement-limited perveance obtained from experiments.

Being unable to apply either theory, an alternative approach is taken. For our model, we approximate the anode current as

$$J_a = j_{i,n} \phi_i A_g = [en_e u_B \exp(-1/2)] \phi_i A_{grid} \quad (30)$$

where $j_{i,n}$ is the ion current density normal to the screen grid that obeys the Bohm condition, u_B is the Bohm velocity, A_g is the grid area, and ϕ_i is the ion transparency of the grid. The ion transparency is naturally a function of the plasma density, the electron temperature, and the inter-grid potential because it is directly related to the sheath in front of the screen apertures. More specifically, by either increasing the applied potential or decreasing the plasma density and the electron temperature, we can increase the size of the screen sheath and thus achieve an increase in the ion transparency fraction of the grid. For simplicity, we model the ion transparency as a linear function of the applied inter-grid potential alone, which is expected to be the dominant factor in the ion extraction mechanism. The actual ion transparency function in our model is then obtained empirically by fitting a set of anode current data,

$$\phi_i = 1.3163 \times 10^{-4} V_{total} + 0.1274 \quad (31)$$

Notice here the ion transparency function strictly depends on the grid geometry and the pattern of the apertures, which means that the Eq. 31 is not universal. From Eq. 31, the ion transparency of the grid is found to be in the same order of the physical opening of the screen grid (~ 0.4), which is deemed a reasonable value for this particular grid set.

The anode current described by Eq. 30 is the ion current. Because there is no internal neutralizer in our discharge chamber, the electron current is forced to flow from the anode to the external cathode to neutralize the ion beam current. If taking account for the accelerator-intercepted current, we can estimate the ion beam current as 95% of the anode current. The thrust performance of an ion thruster can then be related to the ion beam current by

$$\text{Thrust: } T = m_i \Gamma_i c_i + m_n \Gamma_n \bar{c}_n = m_i (J_{beam} / e) (\sqrt{2eV_{net} / m_i}) + m_n [(n_n \bar{c}_n / 4) \phi_n A_{grid}] \bar{c}_n \quad (32)$$

$$\text{Specific Impulse: } Isp = T / (\dot{m}g) \quad (33)$$

where V_{net} is the anode-to-cathode potential, \bar{c}_n is the mean thermal velocity for neutrals, ϕ_n is the physical grid opening for neutral escape, \dot{m} is the mass flow rate, and g is the gravitational constant. The above performance calculations do not include the penalty resulted from beam divergence.

III. Results

The experimental data presented in this section are obtained from an un-optimized version of the ICP RF ion thruster by Busek; they do not represent the performance of the final design. Figure 6 shows the resonant frequency versus flow rate for the ICP discharge without the applied ion extraction potential. As can be seen clearly, our ICP discharge model and the overall circuit model work very well especially at flow rates higher than 2 sccm. The results seen in Fig. 6 are good representation on the validity of our ICP discharge model because it contains no ion extraction element and therefore no data-fitting on the anode current. This result, however, must be used with caution as the resonant frequency is a sensitive quantity and a deviation of 0.01 MHz off the resonant value can result in some increase in reflected power.

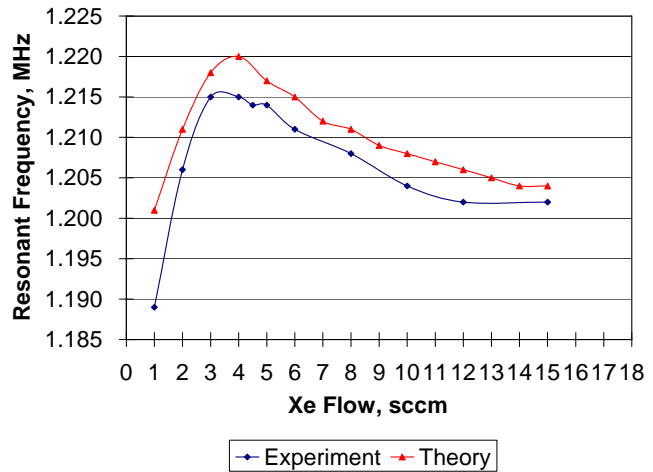


Figure 6. Resonant frequency of the ICP discharge without ion extraction. 250W RF power.

Figure 7 shows the result of our complete model that includes ion extraction. After comparing with experimental data, we found that errors are within 10% or better. These errors are most likely caused by our crude model of ion extraction. As explained previously, the ion extraction mechanism is controlled by the plasma properties and the extraction potential. These quantities affect the shape of the sheath in front of the screen aperture, thus influence the amount and the focusing of the ion current through the sheath. By ignoring the plasma properties in our ion transparency function, we eliminate the effect of plasma density and temperature on ion extractability. Nevertheless, our ion extraction model works very well as seen in Fig. 7 and is deemed adequate overall.

Figure 8 is another validation for our model in terms of the reflected power of the system while the thruster is under operation. As can be seen, we over-predict 20-30% of the reflected power, which means that it is quite possible that we under-predict the absorbed power and therefore under-predict the plasma density. Since our predictions on the resonant frequency are relatively accurate (Fig. 6), this problem could be related to the plasma resistance term R_p seen in Eq. 19. If we correct R_p by multiplying a factor of 0.8, the absorbed power increases and the reflected power would correspond to the experimental data better with errors within 15% or less, as seen in Fig. 8. However, this correction would also decrease the values of ion transparency by about 8% compared to the previous estimates. Since we base this analysis on data-fitting with the anode current, we cannot be certain what levels of ion transparency values are more accurate. This ambiguity cannot be resolved unless we conduct a more thorough simulation on the ion extractability of the grid. Nevertheless, the overall trend of our predicted power reflection is very similar to the actual one in the sense that as more ions are extracted, less chamber plasma is present and more power is reflected. Our approach for the model is therefore deemed correct, but improvements on the ion transparency prediction are needed.

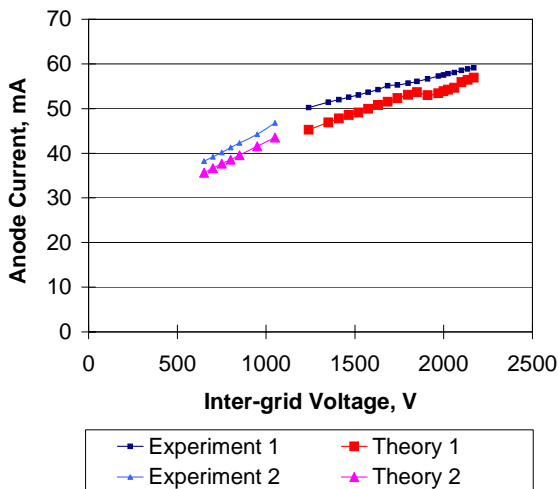


Figure 7. Performance of the ICP RF thruster at resonant frequency. Set 1: 63W RF and 1.39 sccm Xe. Set 2: 51.4W RF and 2.7 sccm Xe.

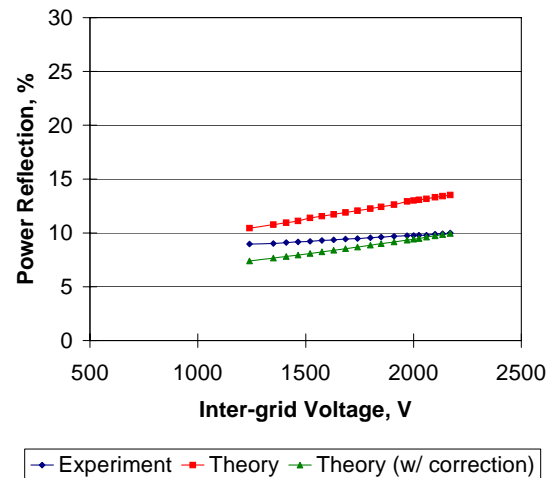


Figure 8. Reflected power of the RF circuit. Thruster operated at resonant frequency. 63W RF and 1.39 sccm Xe.

IV. Conclusion

A simple one-dimensional performance model is developed for an ICP RF ion thruster. Results of the model, including predictions of resonant frequency, reflected power, and anode current, are compared to the experimental data. The ICP discharge model and the associated circuit analysis are deemed valid. The predicted resonant frequencies are accurate to within 0.01MHz. The ion extraction model also yields satisfactory result with accuracy within 10%, but it may be too crude by not accounting for the effect of plasma properties on ion extractability. Predictions on the reflected power of the system are accurate to within 30% without theory correction and 15% with correction. The authors are in the process of acquiring a more detailed ion extraction code, with which the presented ICP discharge model can be improved furthermore and can become a power tool in predicting the performance of an ICP RF ion thruster.

Acknowledgments

The authors would like to thank Mr. Kurt Hohman and Dr. Lynn Olson of Busek, Co., Inc. for providing the experimental data. This project is funded by Busek through NASA SBIR award.

References

- ¹Leiter, H.J. and Feili, D., "RIT 15S – A Radio Frequency Ion Engine for High Specific Impulse Operation," *37th AIAA/ASME/SAE/ASEE Joint Propulsion Conference & Exhibit*, 2001, AIAA 2001-3491.
- ²Leiter, H., Killinger, R., Kukies, R., and Frohlich, T., "Extended Performance Evaluation of EADS ST's 200mN Radio Frequency Ion Thruster," *39th AIAA/ASME/SAE/ASEE Joint Propulsion Conference & Exhibit*, 2002, AIAA 2003-5010.
- ³Brophy, J.R. and Wilbur, P.J., "Simple Performance Model for Ring and Line Cusp Ion Thrusters," *AIAA Journal*, Vol. 23, No. 11, 1985, pp. 1731-1736.
- ⁴Gudmundsson, J.T. and Lieberman, M.A., "Magnetic induction and plasma impedance in a cylindrical inductive discharge," *Plasma Sources Science. Technology journal*, Vol. 6, 1997, pp. 540-550.
- ⁵Szabo, J., Martinez-Sanchez, M. and Batishchev, O., "Fully Kinetic Hall Thruster Modeling," *27th International Electric Propulsion Conference*, Pasadena, CA, 2001, IEPC-01-341.
- ⁶Fridman, A. and Kennedy, L.A., *Plasma Physics and Engineering*, Taylor & Francis Books, Inc., 2004, pp. 17-27, 199-200, 335-342, 593-604.
- ⁷Szabo, J., "Fully Kinetic Numerical Modeling of a Plasma Thruster," Ph.D. dissertation, Department of Aeronautics and Astronautics, Massachusetts Institute of Technology, Cambridge, MA, January 2001, pp. 95-98.
- ⁸Mitchner, M. and Kruger Jr., C.H., *Partially Ionized Gases*, John Wiley & Sons, Inc., New York, 1973, reprint in 1993, pp. 112, 101-124, 214-230.
- ⁹Lieberman, M.A. and Lichtenberg, A.J., *Principles of Plasma Discharges and Materials Processing*, John Wiley & Sons, Inc., New York, 1994, p. 39.
- ¹⁰Grover, F.W., *Inductance Calculations, Working Formulas and Tables*, D. Van Norstrand Company, Inc., NY, 1946, pp. 114-115, 143.
- ¹¹Kong, J.A., *Electromagnetic Wave Theory*, 2nd ed., John Wiley & Sons, Inc., New York, 1990, pp. 145-150.
- ¹²Sutton, G. and Biblarz, O., *Rocket Propulsion Elements*, 7th ed., John Wiley & Sons, Inc., New York, 2001, pp. 679-688.
- ¹³Rovang, D.C. and Wilbur, P.J., "Ion Extraction Capabilities of Very Closely Spaced Grids," *AIAA/JSASS/DGLR 16th International Electric Propulsion Conference*, Nov. 17-19, 1982, AIAA-82-1894,
- ¹⁴Rovang, D.C. and Wilbur, P.J., "Ion Extraction Capabilities of Two-Grid Accelerator Systems," *Journal of Propulsion*, Vol. 1, No. 3, 1985, pp. 1772-179.
- ¹⁵Brophy, J.R., "Effect of Screen Grid Potential on Perveance," appears in "Advanced Ion Thruster Research," NASA CR-168340 (N84-19467), Jan. 1984.